Astron. Astrophys. 355, 1129–1137 (2000)

ASTRONOMY AND ASTROPHYSICS

The structure of the collapsing envelope around the low-mass protostar IRAS 16293-2422⋆

C. Ceccarelli[1], A. Castets[2], E. Caux[3], D. Hollenbach[4], L. Loinard[5], S. Molinari[6], and A.G.G.M. Tielens[7]

[1] Laboratoire d'Astrophysique, Observatoire de Grenoble - B.P. 53, 38041 Grenoble cedex 09, France
[2] Observatoire de Bordeaux, B.P. 89, 33270 Floirac, France
[3] CESR CNRS-UPS, B.P. 4346, 31028 Toulouse cedex 04, France
[4] NASA Ames Research Center, MS 245-3, Moffett Field, CA 94035-1000, USA
[5] Institut de Radio Astronomie Millimétrique, 300 rue de la piscine, 38406 St. Martin d'Hères, France
[6] IPAC, California Institute of Technology, MS 100-22, Pasadena, CA 91125, USA
[7] SRON/Kaypten Institute, P.O. Box 800, 9700 AV Groningen, The Netherlands

Received 6 December 1999 / Accepted 21 January 2000

Abstract. Using H_2O, OI and SiO data, we derive the structure of the collapsing envelope around the low-mass protostar IRAS16293-2422 down to $r \sim 30$ AU. With an accurate model which computes self-consistently the chemical composition, thermal balance and line emission from a collapsing envelope (Ceccarelli et al. 1996), we find that IRAS16293-2422 is a 0.8 $M_\odot$ protostar accreting from the surrounding envelope at a rate of 3.5×10^{-5} $M_\odot$ yr^{-1}, in good agreement with previous studies. The model predicts that the water abundance in the outer (r $\geq$ 150 AU) part of the envelope is 5×10^{-7} with respect to H nuclei, while it is a few times larger at smaller radii (r $\leq$ 150 AU). This enhancement results from the evaporation of icy grain mantles when the temperature exceeds $\sim$ 100 K. The same model can reproduce the observations of the SiO J=2–3 to J=8–7 lines provided the abundance of SiO is 1.5×10^{-8} in the inner region, while it is only 4×10^{-12} in the rest of the envelope. The SiO abundance enhancement in the inner regions is likely due to the evaporation of the grain mantles also responsible for the abundance enhancement of H_2O. The cooling and heating mechanisms of the gas throughout the envelope as derived from the model are discussed, and used to derive the gas temperature profile.

Key words: stars: circumstellar matter – stars: formation – ISM: individual objects: IRAS 16293-2422

1. Introduction

It is now largely accepted that low–mass protostars grow by accreting material from surrounding envelopes. A detailed understanding of the dynamical, thermal, and chemical structure of the collapsing envelopes is therefore necessary to better constrain the processes that lead to the formation of stars and planetary systems. Before such a detailed knowledge can be obtained, however, one has to *find* accreting protostars. Indeed, detection of infall in young stellar objects remains elusive, in spite of recent substantial progress in that direction. The most widely used method to probe infall in protostars is based on observations of the profiles of selected lines from selected molecules. The basic idea consists in using optically thick lines which show self-absorption: in a collapsing envelope such lines are predicted to have the blue-shifted peak less attenuated and therefore brighter than the red-shifted peak (Leung & Brown 1977, Zhou 1992, Choi et al. 1995).

Though very elegant and simple in principle, this method has proved less successful than expected. Gregersen et al. (1997) and Mardones et al. (1997) surveyed 23 and 47 young embedded protostars respectively, and found that the blue peak was stronger than the red one in only $\sim$ 30% of the cases. Using the same method, Williams & Myers (1999) found only 4 collapsing candidates out of 19 sources. In addition, the same source can have a blue peak brighter than the red one in some transitions, but the red one brighter in other transitions – sometimes even with the same molecule (Gregersen et al. 1997). Recently Tafalla et al. (1998) and Williams et al. (1999) found *extended* line asymmetry towards L1544, which is inconsistent with infall. The unreliability of the method is likely due to the simultaneous presence of infall, outflow, rotation and possibly geometrical factors in the same object. To separate the contributions of the various motions is not easy, and may not always be possible. Adelson & Leung (1988), Walker, Narayanan & Boss (1994), and Narayanan & Walker (1998) tried to separate rotation from infall by comparing the emission around the source to that on–source. In summary the analysis of the line(s) profile(s) alone is not enough to assess whether a source is collapsing. Each *candidate collapsing source is on a trial based on circumstantial*

Send offprint requests to: Cecilia Ceccarelli; LAOG; (Cecilia.Ceccarelli@obs.ujf-grenoble.fr)

⋆ Based on observations with ISO, an ESA project with instruments funded by ESA Member States (especially the PI countries: France, Germany, the Netherlands and the United Kingdom) with the participation of ISAS and NASA.

evidence: with increasing evidence raising the probability that the collapse is detected.

In the absence of a reliable method to trace infall, no attempt to model the thermal structure of a "real" collapsing envelope has been made so far, though a few simple theoretical models exist (Ceccarelli et al. 1996, hereinafter CHT96; Doty & Neufeld 1997). Those models predict that the major coolants of the warm gas in the inner regions of the collapsing envelope are the pure rotational lines of H_2O and the fine structure lines of OI, in the far-infrared. With the Infrared Space Observatory (ISO: Kessler et al. 1996) we can now observe some of these lines, and use them to study young sources in which infall is suspected. This provides an approach to the infall problem radically different from those used until now.

In this paper we consider the case of IRAS16293-2422 (hereafter IRAS16293), a well studied low–mass protostar, located in the ρ Ophiucus cloud complex (see van Dishoeck et al. 1995 for a review on this source). IRAS16293 (L = 27 $L_\odot$, distance = 160 pc) was the first low–mass protostar where hints for infall were found (Walker et al. 1986). Since then, although the evidence for collapse presented in Walker et al. has been severely questioned, new data and different analysis methods sustained the hypothesis that the envelope surrounding IRAS16293 is undergoing collapse (Zhou 1995, Narayanan et al. 1998). Here, we analyse old and new observations of H_2O, OI and SiO line emission towards IRAS16293. The data are used to reconstruct the thermal structure of the envelope on the scale of a few tens astronomical units using the model developed by CHT96. We derive various physical parameters of the inner envelope including the gas heating and cooling rates and mechanisms, the mass infall rate, the mass of the protostar, the gas phase abundances of the molecular species considered, and an estimate of the amount of ice evaporated as the collapsing gas approaches the protostar.

2. Observational data set

First, we present the observations which are used for the modeling. All the data used in this paper refer to the center of IRAS16293 at α(1950) = $16^h29^m20\overset{s}{.}9$ and δ(1950) = $-24°22'13''$.

A low–resolution (R=$\lambda/\Delta\lambda \sim 200$) spectrum covering the wavelength range 45 μm – 200 μm was obtained with the *Long Wavelength Spectrometer* (LWS – Clegg et al. 1996) on board the ISO satellite. Nine rotational lines of H_2O and the 63 μm fine structure line of OI were extracted from the spectrum (Ceccarelli et al. 1998a, 1999). In addition, we searched – but unsuccessfully; see Fig. 1 – for two high-lying rotational transitions of the ground vibrational state of H_2O with the *Short Wavelength Spectrometer* (SWS – de Grauuw et al.1996) also on board ISO. Those correspond to the $4_{4,1} - 3_{1,2}$ and $5_{5,0} - 4_{2,3}$ transitions at 31.77 and 22.64 μm respectively. The SWS observations were performed in the AOT02 mode. While the LWS aperture is about 80″ for all the lines considered, that of SWS is 20″ × 27″ at 31.77 μm and 14″ × 27″ at 22.64 μm. The data were reprocessed through the Off–Line–Package (OLP) version 7; final analysis was done using the standard ISO Spectral Analysis Package (ISAP V1.5). The absolute flux calibration is accurate to 20%. Measured line fluxes or upper limits are reported in Table 1.

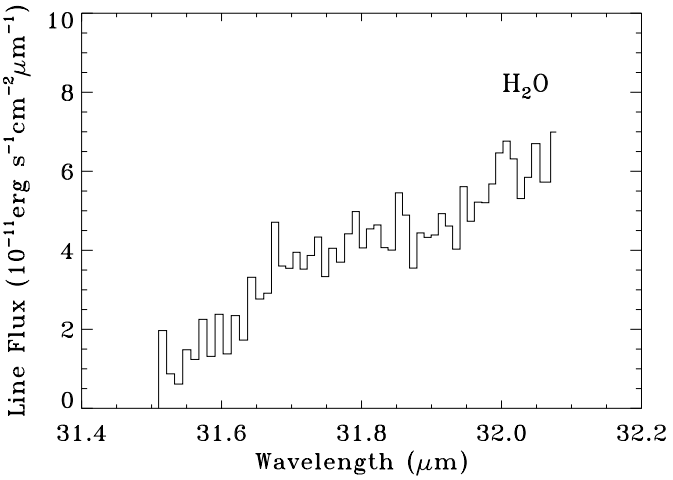

Fig. 1. ISO spectrum around the H_2O line at 31.77 μm. No line is detected.

Table 1. Fluxes of the H_2O and OI lines detected towards IRAS16293. The flux of the H_2O lines at 132 μm is different from that reported in Ceccarelli et al. (1999); the H_2O line at 108 μm was not quoted in Ceccarelli et al.. These differences are a result of the improvements in the processing and analysis of ISO-LWS data conducted by the ISO-LWS Instrument Team.
The statistical errors in the determination of the line fluxes in the LWS range are usually around $\sim 2\times10^{-13}$erg s^{-1} cm^{-2}. All the lines reported in the table are at least 2σ detections. The errors reported in the table include the uncertainty in the definition of the baseline, that is the main source of error in the estimate of the line fluxes (even when a line is clearly detected). This is due to the overcrowded line spectrum of IRAS16293, in which sometimes lines are merged together or just barely separated (see also Ceccarelli et al. 1998b). The upper limits on the H_2O lines at 31 and 22 μm are at 3 σ.

λ (μm)	Transition	Line Flux 10^{-12}erg s^{-1} cm^{-2}
180.5	H_2O $2_{21} - 2_{12}$	0.9 ± 0.4
179.5	H_2O $2_{12} - 1_{10}$	2.9 ± 0.6
174.6	H_2O $3_{03} - 2_{12}$	2.5 ± 0.6
138.5	H_2O $3_{13} - 2_{02}$	0.9 ± 0.7
132.4	H_2O $4_{23} - 4_{14}$	0.7 ± 0.7
108.1	H_2O $2_{21} - 1_{10}$	1.7 ± 0.6
101.0	H_2O $2_{20} - 1_{11}$	1.3 ± 0.6
90.0	H_2O $3_{22} - 2_{11}$	0.5 ± 0.5
75.4	H_2O $3_{21} - 2_{12}$	2.7 ± 1.0
31.77	H_2O $4_{41} - 3_{12}$	$\leq$0.5
22.62	H_2O $6_{52} - 5_{23}$	$\leq$0.07
63.2	OI $^3P_1$-$^3P_2$	6.5 ± 0.9

Using the IRAM 30–m and SEST 15–m telescopes, Castets et al. (in prep.) obtained large–scale SiO J=2–1, J=3–2 and J=5–4 maps around IRAS16293. Those maps show strong SiO emission at the far end lobes of the outflow, while only weak SiO emission is observed on the source itself. Remarkably the J=5–4

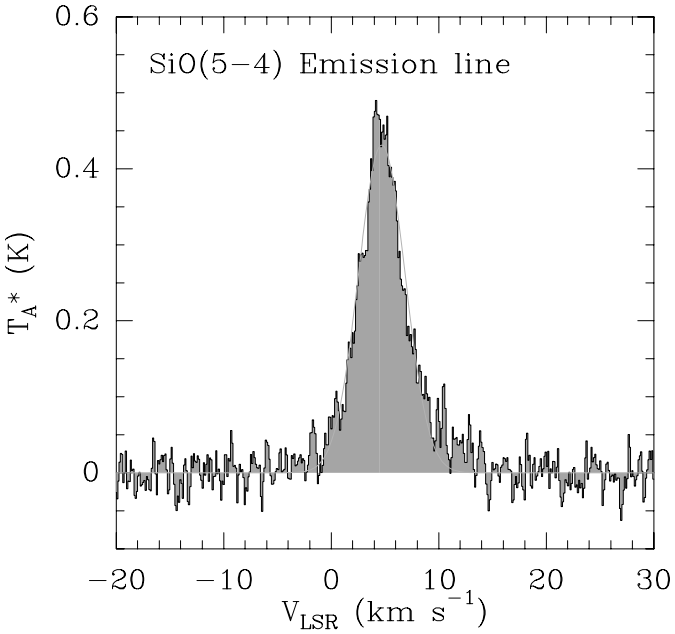

Fig. 2. SiO(5-4) spectrum obtained at SEST towards IRAS16293.

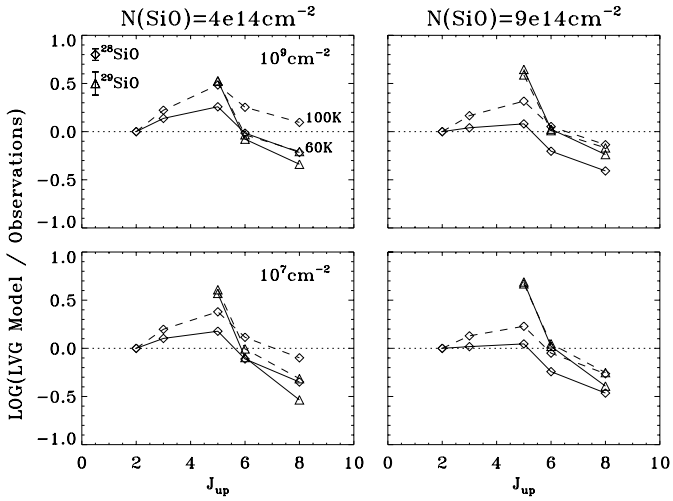

Fig. 3. The ratio between the LVG modeling predictions and the observations as function of the J_{up} of the transition. The observations include both our observations at J_{up}=2,3 and 5 and the observations by Blake et al. (1994) at J_{up}=5,6 and 8. Diamonds represent the ^{28}SiO lines and triangles the ^{29}SiO lines. Left panels report computations for N(SiO)=4×10^{14} cm^{-2}, equivalent to the lowest N(SiO) that gives optically thick lines. Right panels report the case discussed by Blake et al., i.e. N(SiO))=9×10^{14} cm^{-2}. Dashed curves refer to a temperature of 100 K and solid curves to 60 K. Upper panels report computations with a density of 10^9 cm^{-3}, while lower panels report a density of 10^7 cm^{-3}. The figure shows that the LVG model is unable to reproduce all the observed lines simultaneously, no matter what N(SiO) or density or temperature is taken for the gas.

emission towards the source is concentrated in one IRAM 10″ beam, while no emission is detected at the adjacent positions. The high signal-to noise SiO J=5-4 profile, obtained at SEST towards the center (Fig. 2), has a FWHM of 5 km s^{-1}. We will also make use of the observations by Blake et al. (1994) of the J=5–4, J=6–5, and J=8–7 transitions of ^{28}SiO and ^{29}SiO.

3. LVG modeling of the data

Ceccarelli et al. (1999) modeled the H_2O observations of IRAS16293 using an LVG code. They concluded that the emitting region was small ($\sim$ 2-3" $\sim$ 200 AU), warm ($\sim$ 100 K), and dense ($\geq 10^7$ cm^{-3}): the derived H_2O column density is $\geq 10^{16}$ cm^{-2}. However, they showed that LVG modeling of the H_2O lines is unable to fully reproduce the observations, and that it is only a crude description of the reality.

Using the J=5–4, J=6–5, and J=8–7 transitions of ^{28}SiO and ^{29}SiO emission Blake et al. (1994) estimate a SiO emitting region smaller than $\sim 3''$, where the gas is warm ($T_{rot} \geq 60$ K) and dense, and whose SiO column density is larger [1] than 9×10^{14} cm^{-2}. Also in this case, LVG modeling cannot fully reproduce the observations (Fig. 3). Nevertheless, LVG modeling suggests that the H_2O and SiO lines might have a common origin, an hypothesis that we will fully exploit in the next section.

4. Modeling the collapsing envelope

IRAS16293 is a fairly complex system where several components coexist (see van Dishoeck et al. 1995 and references therein). The question of the exact origin of the observed OI, H_2O and SiO emission therefore immediately arises. For the densities and temperatures derived above, there are *a priori* three possibilities. The emission could come from the collapsing envelope itself, from a disk, or from shocks – either at the interface between the envelope and the jet/wind emitted by the central object or within the disk. Ceccarelli et al. (1999) presented statistical arguments favoring the collapsing envelope hypothesis for the H_2O lines. We are now going to show that all the data presented in this article are consistent with this hypothesis. Furthermore, we will show how these data can be used to reconstruct the thermal structure of the inner regions of the envelope.

4.1. General considerations

In Sect. 4.2 – 4.5 we will make use of the accurate CHT96 model that describes a collapsing envelope to interpret the OI, H_2O and SiO observations. First, however, we give some simple arguments, based on the H_2O and SiO observations, showing the plausibility of the collapsing envelope hypothesis. Such simple arguments can also be used to derive "order-of-magnitude" estimates of some physical parameters of the system, like the central mass and the mass accretion rate.

– The SiO emission originates at a distance of a few hundred AUs from the central source, and the velocity dispersion of the

[1] Blake et al. report a ^{28}SiO column density averaged on their 20" beam equal to 2×10^{13} cm^{-2}, which becomes equal to 9×10^{14} cm^{-2} when considering the 3" extent.

gas is $\sim$ 5 km s^{-1}. This is compatible with gas free–falling towards a $\sim$ 1 M$_\odot$ central object.
– The temperature of the gas derived from the H_2O and SiO lines is $\sim$ 60-100 K in a region with size of $\sim$ 150 AU. If the dust is optically thick, the dust temperature profile of a sphere heated by a central source of radiation can be shown to be roughly given by

$$\mathrm{T}_{dust}(r) = 75 \left(\frac{\mathrm{L}_\star}{27\mathrm{L}_\odot}\right)^{1/4} \left(\frac{\mathrm{r}}{150\mathrm{AU}}\right)^{1/2} \mathrm{K}. \quad (1)$$

CHT96 showed theoretically that in the collapsing envelopes surrounding low–mass protostars, the temperature of the gas followed closely that of the dust. The gas temperature derived from the SiO observations is therefore in principle compatible with the hypothesis of gas warmed up by the 27 L$_\odot$ central source.
– The H_2O observations show that at a few hundred AUs from the central source, the gas has a volume density larger than 10^7 cm^{-3}. In the "inside-out" model (Shu 1977), the density n in the free-falling region can be described by

$$n = 6\times10^6 \left(\frac{\dot{\mathrm{M}}}{10^{-5}\mathrm{M}_\odot\mathrm{yr}^{-1}}\right) \left(\frac{\mathrm{M}_\star}{\mathrm{M}_\odot}\right)^{-0.5} \left(\frac{\mathrm{r}}{150\mathrm{AU}}\right)^{-1.5} \mathrm{cm}^{-3} \quad (2)$$

where $\dot{\mathrm{M}}$ is the mass accretion rate, and M$_\star$ the mass of the central object. A density at 150 AU larger than 10^7 cm^{-3} therefore points to a mass accretion rate larger than $\sim 2\times 10^{-5}$ M$_\odot$ yr^{-1}.

4.2. Description of the model

CHT96 developed a model which computes self-consistently the thermal structure and the OI, H_2O and CO line spectrum of the collapsing envelopes around low-mass protostars within the "inside-out" framework. This model accounts for the chemical structure of the envelope which changes with the age of the protostar. The model computes the abundances of the three main coolants of the gas in the envelope, namely atomic oxygen, water and carbon monoxide. CO is a very stable molecule; its abundance only depends on the amount of carbon in the gas phase. Assuming that carbon is less abundant than oxygen, essentially all gas phase carbon is incorporated in CO. H_2O is formed in the gas phase (when the gas temperature reaches $\sim$ 220 K, endothermic reactions open efficient routes to water production) and can be injected into the gas phase by the evaporation of icy grain mantles (when the dust temperature exceeds 100 K). The water abundance in the cold ($\leq$ 220 K) part of the envelope and the amount of ice in the grain mantles are *a priori* poorly known parameters. OI is also a stable species, which disappears only in the inner regions (where T $\geq$ 220 K) where all oxygen reacts to form water molecules.

The gas in the innermost regions of the envelope ($\leq$ 200 AU) is mostly heated through compression of the gas and through absorption by water of NIR photons emitted by the warm inner dust, followed by collisional de-excitation of the excited water molecules. The key parameters controlling the gas compressional heating are the gas density and velocity dispersion, which – in the inside-out framework – are directly set by the mass accretion rate and central mass. The abundance of water in the inner regions regulates the heating due to the absorption of NIR photons. The gas cooling is expected to be dominated by the rotational line emission of CO in the outer part of the envelope ($\geq$ 1000 AU) and H_2O in the inner regions ($\leq$ 200 AU). In the intermediate parts, the fine structure line of OI at 63 μm and the rotational lines of CO dominate the cooling. The abundances of OI and CO are therefore also key parameters of the model. In all, the model depends on six parameters:
– The central mass of the protostar M$_\star$,
– The mass accretion rate $\dot{\mathrm{M}}$,
– The initial (pre-infall) abundances of gaseous OI: X(OI), gaseous CO: X(CO), and gaseous water: $X_{out}(H_2O)$,
– The amount of water evaporated from the grain mantles $X_{ev}(H_2O)$.

The values of the central mass and of the accretion rate are the targets of our study; they will be considered free parameters of the model. The determination of the abundance of gaseous OI in cold molecular clouds has long relied on the results of chemical models of molecular clouds. According to such models, a large fraction of the gaseous oxygen is locked into CO molecules (e.g. Lee et al. 1996). Molecular oxygen is observationally known to be unimportant (Pagani et al. 1993, Maréchal et al. 1997 and Olofsson et al. 1998) and the remainder of the oxygen is generally agreed upon to be in atomic form.

Recent observations in some molecular clouds suggest that most of the oxygen in the gas phase is indeed in the form of OI (Poglitsch et al. 1996; Baluteau et al. 1997; Kraemer et al.1998; Caux et al. 1999). Moreover, CO is heavily depleted (Lefloch et al. 1998; Kramer et al. 1999; Caux et al. 1999) in these clouds. Caux et al. (1999) observed two fine structure lines (63 and 145 μm) of OI towards the molecular cloud L1689N, in which IRAS16293 is embedded. They find that almost 100% of all the oxygen in the gas phase is in the form of OI, while the abundance of CO is not larger than 10^{-5} with respect to H nuclei. We will therefore use X(OI) = 2.5 $\times$ 10^{-4}, and X(CO) = 10^{-5}. It is plausible that a large fraction of the CO is frozen out in a molecular ice. Once the dust temperature exceeds 20 K the CO trapped in the grain mantles evaporates and X(CO) = 10^{-4}. However, since the CO lines are the dominant gas coolants only in the outer regions of the envelope, this parameter does not affect the computed OI and H_2O line intensities. The predicted CO line intensities are relatively weak and the high J lines are predicted to be unobservable with the present instrumentation. Note that the bright high J CO lines observed in IRAS16293 are thought to arise in the shocks at the interface between the outflow and the surrounding static medium (Ceccarelli et al. 1998a).

With regard to the water abundance in the cold part of the envelope, Caux et al. (1999) find an upper limit to the H_2O abundance in L1689N of 6 $\times$ 10^{-7} relative to H nuclei. The abundance of water in the cold part of the envelope $X_{out}(H_2O)$ was therefore varied between 1.5 $\times$ 10^{-7} (see CHT96) and 5 $\times$ 10^{-7}. Finally, the amount of ice trapped in the grain mantles

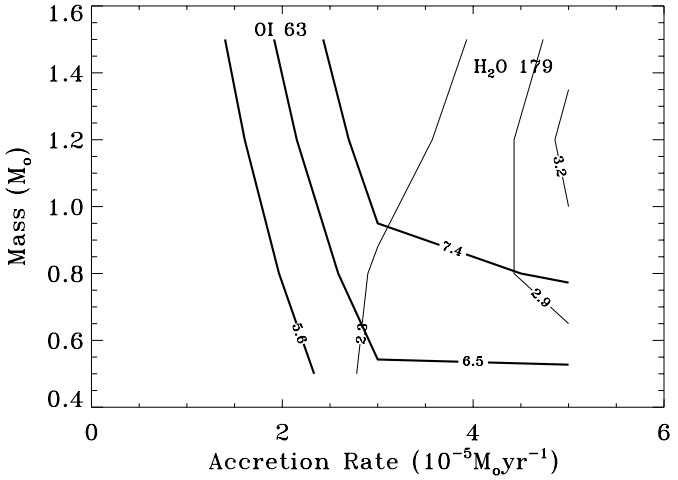

Fig. 4. Model predictions of the H_2O 179 μm (thin) and OI 63 μm (thick) lines as function of the mass accretion rate and the mass of the central object. The three curves represent the observed line fluxes in units of 10^{-12} erg cm^{-2} s^{-1} plus their low and high limits given by the errors (1 σ) in Table 1. The abundance of H_2O in the cold outer envelope is equal to 5×10^{-7}. The H_2O 179 μm line is relatively insensitive to the amount of H_2O ice, $X_{ev}(H_2O)$, because most of the emission arises from cooler material.

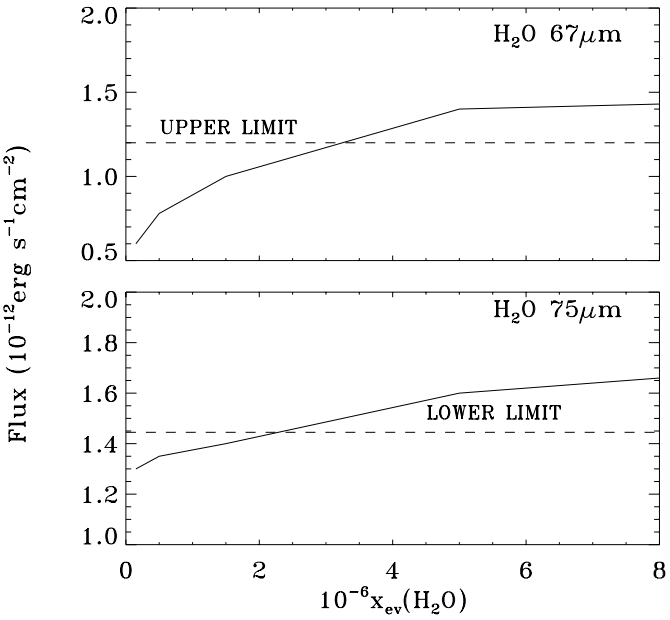

Fig. 5. Model predictions of the H_2O 75.38 μm ($3_{21} - 2_{21}$) and 67.27 μm ($3_{30} - 3_{03}$) lines as function of the amount of water evaporated from the ice mantles and injected in the gas phase. In the lower panel the lower limit, multiplied by the calibration uncertainty, of the 75.38 μm *observed* flux is shown as dashed line. On the contrary, the 67.27 μm line is undetected by our observations. The dashed line of the upper panel shows the 3 σ upper level on the 67.27 μm flux, multiplied by a factor which accounts for the calibration uncertainty (20%).

and released into the gas phase is left as a free parameter since there are no direct observations of its value towards this source.

4.3. Constraining the model parameters

The H_2O $2_{1,2} - 1_{0,1}$ transition at 179 μm and the OI transition at 63 μm have relatively low upper level energies ($\sim$80 and 230 cm^{-1} respectively) and large absorption coefficients. They are therefore likely to become optically thick very quickly in the outer regions, and to be largely insensitive to the value of $X_{ev}(H_2O)$, which only affects the emission from the inner regions. These lines can therefore be used to constrain $M_\star$, $\dot{M}$, and $X_{out}(H_2O)$.

Fig. 4 shows the H_2O 179 μm and the OI 63 μm line fluxes as function of the mass accretion rate and central mass for $X_{out}(H_2O) = 5 \times 10^{-7}$. A similar plot was obtained for the lower value of $X_{out}(H_2O) = 1.5 \times 10^{-7}$. The observed line fluxes agree better with the higher value of water abundance in the outer parts of the envelope. A lower value of $X_{out}(H_2O)$ would produce too little 179 μm flux and too much OI 63 μm flux. The comparison of the observed fluxes with Fig. 4 implies a mass accretion rate larger than $\sim 3\times 10^{-5}$ $M_\odot$ yr^{-1} and a central mass lower than $\sim$ 0.9 $M_\odot$. The best fit obtained using all the other low-lying observed H_2O lines gives $M_\star$=0.8 $M_\odot$ and $\dot{M}$=3.5$\times$ 10^{-5} $M_\odot$ yr^{-1}.

The low-lying water lines are sensitive to the outer regions of the envelope while they are insensitive to the amount of ice evaporated in the inner region where $T_{dust} \geq 100$ K. Water lines with upper level energies of more than 200 K, on the other hand, are likely to originate in the inner regions of the envelope and to be sensitive to the amount of water injected in the gas phase when the icy mantles evaporate. The $3_{21} - 2_{21}$ line of H_2O at 75.38 μm (E_{up}=212 cm^{-1}), along with other water lines with similar high energy upper levels, can therefore be used to constrain the value of $X_{ev}(H_2O)$. In Fig. 5 we show the model predictions as a function of $X_{ev}(H_2O)$ for the 75.38 μm line and the 67.27 μm line (E_{up}=285 cm^{-1}), which is *undetected* in our spectrum of IRAS16293. The 75.38 μm line has been chosen here because, among the detected water lines, it is the one giving the most robust constraint on the icy mantle evaporation: $X_{ev}(H_2O) \geq 2 \times 10^{-6}$. Unfortunately this line becomes easily optically thick and it is therefore insensitive to the amount of evaporated water for values larger than $\sim 4\times10^{-6}$. Neverthless, its measured flux implies that an extra injection of water takes place when $T_{dust} \geq 100$ K: there is a region where icy mantles evaporate. On the other hand, the upper limit $X_{ev}(H_2O) \leq 3.5\times 10^{-6}$ derived from the 67.27 μm line suggests that the amount of such evaporated ice is less than 1% of the oxygen in the gas phase. In the following we adopt $X_{ev}(H_2O) = 3\times10^{-6}$ to derive the thermal structure of the envelope around IRAS16293 and we will discuss the implications due to this uncertainty.

In summary, the best fit to the data is obtained for the following parameters:
– X(OI) = 2.5 $\times$ 10^{-4},
– X(CO) = 10^{-5} – 10^{-4},
– $\dot{M}$ = 3.5 $\times$ 10^{-5} $M_\odot$ yr^{-1},
– $M_\star$ = 0.8 $M_\odot$,
– $X_{out}(H_2O) = 5 \times 10^{-7}$,
– $X_{ev}(H_2O) = 3 \times 10^{-6}$.

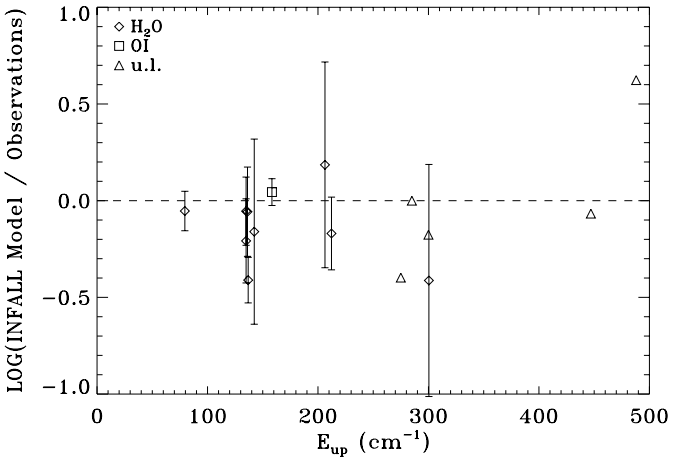

Fig. 6. Comparison between the best-fit model (see text) and the observations of the H_2O (diamonds) and OI lines (square), as function of the upper level energy of each transition. The triangles report upper limits to not detected H_2O lines. The error bars do not include the uncertainty on the flux calibration, which would shift all the points at the same time, by not more than 20%. The upper limit at $E_{up} \sim 500$ cm^{-1} is the 31.77 μm line, which originates at $\sim$20 AU from the center where the spherical symmetry implicit in our model may break down (see text).

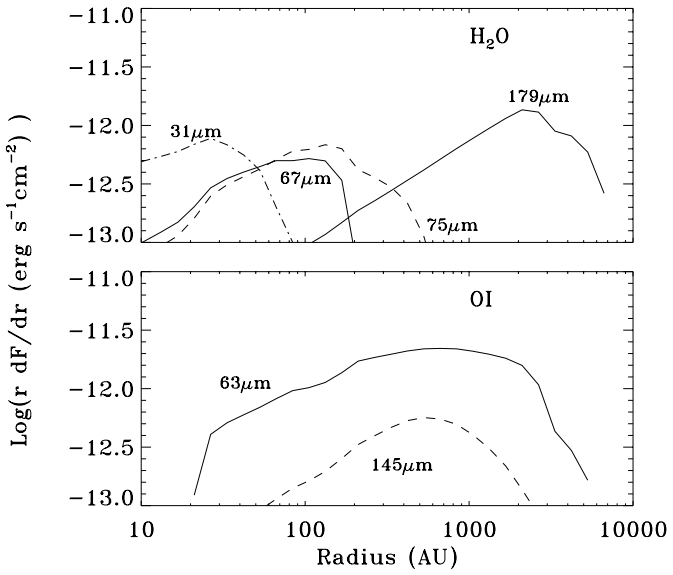

Fig. 7. r(dF/dr) versus the radius r of selected water (top) and OI (bottom) lines. F is the observed flux in the lines; the ISO-LWS beam extends to 5500 AU.

Within the observational uncertainties, the predictions of the model with those parameters are consistent with the H_2O and OI observations (Fig. 6); the only exceptions are the 31.77 and 22.62 μm lines, which are respectively four and twenty times fainter than predicted by our model. We will discuss below the reason of this discrepancy.

Fig. 7 shows the contribution to the observed flux for some of the OI and H_2O lines, as a function of the radius. As expected, the OI 63 μm line traces the region between 300 and 3000 AU; the H_2O 179 μm line traces the outer part (r$\geq$ 2000 AU) of the envelope. The regions at $\sim$ 150 AU, where the grain mantles evaporate, are traced by lines with higher upper level energies, like the OI line at 145 μm or the H_2O lines at 75 μm and 67 μm. Finally, the innermost regions of the envelope, at $\leq$ 40 AU, are traced by the high lying water line at 31.77 μm ($E_{up} \sim 500$ cm^{-1}), while the 22.62 μm line with $E_{up} \sim 900$ cm^{-1} traces even closer regions at less than 10 AU.

In principle the discrepancy between the predicted and observed flux of the 31.77 and 22.62 μm lines can be caused either by the break down at $r \leq 30$ AU of the spherical symmetry implicit in our model, or by an overestimate of water production at $r \leq 30$ AU. To check the first possibility we ran a model in which we start the integration at r = 30 AU. As expected, this case predicts the 31.77 and 22.62 μm line fluxes in agreement with what (not) observed. On the contrary, a model in which we suppressed the formation of water via endothermic reactions predicts a 22.62 μm line much weaker and compatible with our upper limit, but a 31.77 μm line still a factor of three higher than observed. We therefore conclude that our model is a good description of the envelope surrounding IRAS16293 for $r \geq 30$ AU, while at smaller radii the spherical symmetry severely breaks down. It is difficult to say whether including a distortion due to the rotation (e.g. Terebey et al. 1984) will be enough to account for the lack of the 31.77 and 22.62 μm line emission. A major ingredient which is certainly missing in our CHT96 model is the presence of a disk. Infall could abruptly terminate inside 30 AU as it impacts the disk. The disk and accretion shock may be weak in these lines. High resolution interferometric observations at submillimeter and millimeter wavelengths, capable to penetrate the obscuring envelope around IRAS16293, are necessary to address the issue. The Atacama Large Millimeter Array (ALMA), reaching tenths of arcsecs of resolution, will image the $r \leq 30$ AU inner region and probably help to determine the presence of a disk and its accretion shock.

4.4. Results

Using the parameters derived above, we can reconstruct the structure of the envelope at $r \geq 30$ AU. The corresponding gas density, gas temperature, and dust temperature profiles are shown on Fig. 8. A large fraction of the envelope is undergoing collapse: regions up to around 3000 AU are falling towards the interior. The gas is tightly coupled with the dust, the temperature difference between the two never exceeds a few Kelvins. At large distances ($r \geq 400$ AU) the gas is colder than the dust. Between $\sim$150 and 400 AU the gas becomes warmer (because of the increasing opacity of the OI and CO lines), until, at $\sim$150 AU, the water content in the gas phase increases by a factor six because of the evaporation of the water ice in the grain mantles. At this distance, the temperature of the gas drops by few Kelvins as the water cooling becomes more efficient. Note that since most water lines are optically thick at $\sim$150 AU, increasing the amount of water injected in the gas phase to 10% instead of the

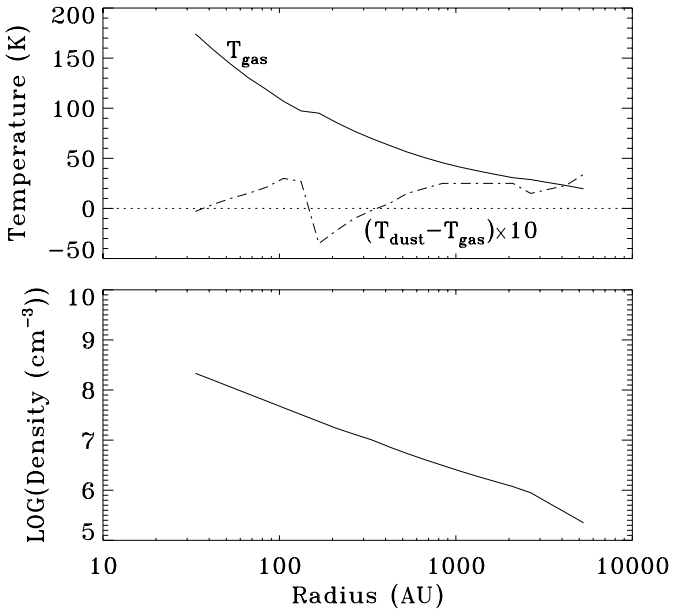

Fig. 8. Upper panel: the gas temperature profile (solid line) as computed by the model which best fits the OI and H_2O line observations. The dashed-dotted line shows the difference between the dust and gas temperatures multiplied by a factor 10, to make the difference visible on the plot. The small drop in the gas temperature at ~ 150 AU is due to the mantle ice evaporation which injects large amounts of water in the gas phase. Lower panel: the density profile computed by the same model. The break in the density power law at $\sim$3000 AU indicates the transition between the collapsing (n$\propto$ r$^{-3/2}$) and static regions (n$\propto$ r^{-2}) of the envelope.

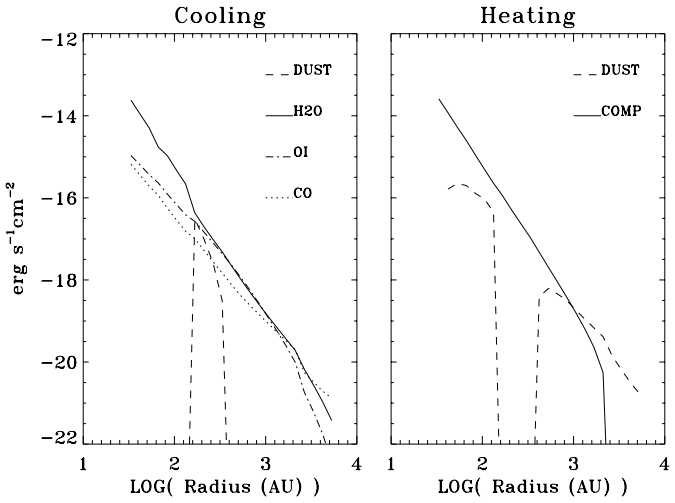

Fig. 9. The cooling (left) and heating (right) rates versus the radius, as computed by the model which best fits the OI and H_2O line observations. Left panel: water rotational line emission (solid line), gas-grain collisions (dashed line), OI 63μm line emission (dashed-dotted line) and CO rotational line emission (dotted line). The jumps in the water cooling rate at ~ 150 AU is caused by the increase of water abundance because of mantle ice evaporation. Right panel: the heating is dominated by the compression of the gas collapsing towards the center (solid line) and the gas-grain collisions (dashed line). The latter appears as a heating mechanism when the dust is warmer than the gas and as a cooling mechanism when the gas is warmer than the dust.

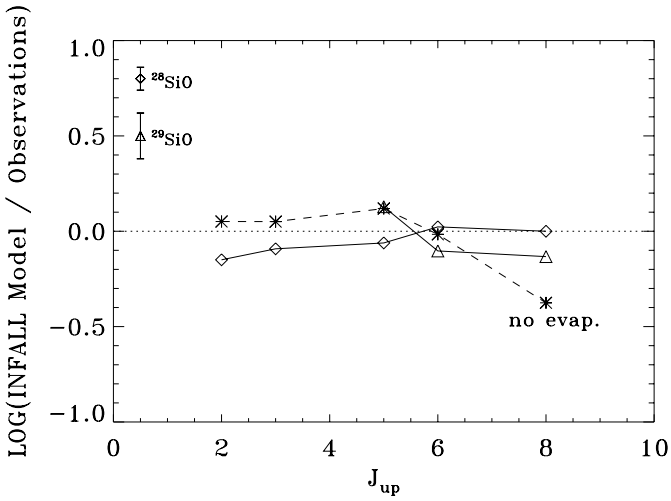

Fig. 10. Ratios between the SiO predicted and observed fluxes as function of J_{up}. Star symbols and dashed line compare the ^{28}SiO observations with the best-fit model in which the SiO abundance is constant across the envelope and equal to 1×10^{-10}. Diamonds and triangles are respectively the comparison of the ^{28}SiO and ^{29}SiO observations with respect to the best-fit predictions of a two component model (see text). The errors on the observations are shown in the upper left corner.

adopted 1% would not change the computed (gas) temperature profile by more than few Kelvins.

The heating and cooling of the gas throughout the envelope are shown in Fig. 9. Gas heating is dominated by compression, except in the outer regions (r $\geq$ 1000 AU), where the dust is warmer than the gas and the collisions between dust and gas are the major heating mechanism. In the intermediate regions of the envelope the dust can be colder than the gas and the gas-grains collisions contribute to the cooling of the gas in those regions. The cooling is dominated by the water rotational line emission in a large fraction of the envelope, larger indeed than expected from our previous CHT96 models. This is due to the relatively higher water abundance (X_{out}(H_2O) = 5×10^{-7}) in the cold parts of the envelope with respect to the value adopted by CHT96 (X_{out}(H_2O) = 1.5×10^{-7}). The OI and CO lines contribute significantly to the cooling only at r $\geq$ 300 AU and r $\geq$ 1000 AU respectively.

4.5. SiO emission from the collapsing envelope

Using the same parameters as above, we can compare the predictions of the model to the SiO observations. First, we assumed that the abundance of SiO, X(SiO), was constant throughout the envelope. The model failed to reproduce the data for any value of X(SiO); for instance, X(SiO) = 10^{-10} (Fig. 10) predicts an intensity for the J=8-7 transition too high, and an extent for the J=6-5 and J=5-4 too large.

We then considered a model where the abundance of SiO was not constant throughout the envelope. In the outer regions, the abundance X_{out}(SiO) was taken close to the values found in cold clouds. Closer to the center, however, an extra–amount

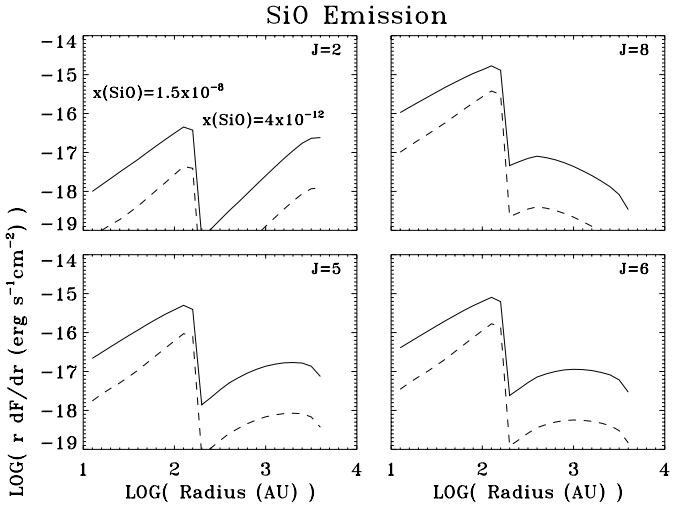

Fig. 11. The best-model predictions of the ^{28}SiO (solid lines) and ^{29}SiO (dashed lines) line emission as function of the distance from the central source, for J=2-1, J=5-4, J=6-5 and J=8-7 respectively.

X_{ev}(SiO) could be injected into the gas phase by the evaporation of the dirty ices at T_{ev}. The best fit to the data is obtained for X_{out}(SiO)=4×10^{-12}, X_{ev}(SiO)=1.5×10^{-8} and T_{ev} = 100 K. For those values, the model accounts successfully for both the ^{28}SiO and the ^{29}SiO observed fluxes (Fig. 10), and predicts that the bulk of the J=5-4 emission (Fig. 11) arises at a distance of about 150 AU from the central source, where the infall velocity is 2.8 km s^{-1}. This is in excellent agreement with the observed SiO J=5-4 linewidth of $\sim$ 5 km s^{-1}.

5. Discussion

The values of the central mass and mass accretion rate in IRAS16293 found here are in reasonable agreement with those found by Narayanan et al. (1998) (2.9×10^{-5} M$_\odot$yr^{-1} and ~ 1.7 M$_\odot$) using a line profile analysis. The fact that two analyses based on such different methods give similar results suggests that our model describes correctly the infall in IRAS16293, and that "inside-out" collapse works reasonably well in describing the dynamical structure of low–mass infalling envelopes.

According to our model, gas and dust are thermally coupled in infalling envelopes, the difference being within few%. Water is indeed found to be the major actor in the thermal balance of the gas throughout most of the collapsing envelope.

An important result of the model is the key role played by the evaporation of ices near the central object. The amount of water released into the gas phase by evaporation of the grain mantles is few times larger than that present in the cold ($T_{dust} \leq 100$ K) part of the envelope. Yet our data suggest that the evaporated water is less than $\sim$1% of the total oxygen present in the gas phase, a rather small number when compared to the estimates of the ice abundances towards other protostars (10 times higher on average – Chiar et al. 1995; Gerakines et al. 1999). Whether IRAS16293 is an exception in this respect is probably premature to assess, more sensitive observations of water lines are needed to settle this point.

Another interesting result from our model is the release of SiO from the dust grains at high temperature. The abundance of evaporated SiO derived from the model is of the order of that observed towards the shocks in outflows, i.e. 10^{-8} (Bachiller 1996; Lefloch et al. 1998). SiO enhancements observed towards outflows might also result from the (partial) destruction by ion sputtering of the grain mantles rather than from the destruction of grain cores. A second implication, more subtle but even more important from a practical point of view, is that since the *evaporated* SiO originates in the inner regions of the envelope, where the free-fall velocity is several km s^{-1} and therefore much larger than the velocities in the outer envelope, the long sought signature of the collapse is probably easier to detect in the high J (J$\geq$5) transitions of this molecule than in other molecules which radiate primarily in the outer envelope. As a follow up, other molecules, which are known to be abundant in the ices and have transitions in the millimeter to submillimeter range, should be good tracers of the collapse: probably the recently discovered D_2CO belongs to this set (Ceccarelli et al. 1998b).

In their spectral survey towards IRAS16293, van Dishoeck et al. (1995) noticed the presence of a warm (~ 80 K) and dense ($\sim 10^7$ cm^{-3}) component at less than 1500 AU (10″) from the center, enriched in CH_3OH, H_2CO, and Si- and S-bearing molecules. They argue that this warm gas is the result of the interaction between the outflow and the envelope surrounding IRAS16293, and that the enrichement results from sputtering of the dust grains due to some gentle shocks. Indeed the presence of shocks associated with the outflows emanating from IRAS16293 is well documented by many observations. However, no observations at angular scales smaller than $\sim$ 6" are so far available (van Dishoeck & Blake 1998) and we demonstrated in the present work that the observed SiO emission is also compatible with heating from the central source and the evaporation of dirty ice mantles in the infalling dust and gas, causing SiO emission from a region smaller than 3". Furthermore, our suggestion is that also the other Si- and S-bearing and CH_3OH and H_2CO molecules have a similar origin, i.e. they are molecules initially trapped in the mantles and released into the gas phase because of the evaporation of the dirty ices.

6. Conclusions

We successfully modeled the OI, H_2O and SiO line emission observed towards the low-mass protostar IRAS16293 by means of an accurate model previously developed (CHT96), which self-consistently computes the thermal structure and line emission from a collapsing envelope, within the "inside-out" collapse paradigm of Shu (1977). We found that the envelope around IRAS16293 is collapsing towards a 0.8 M$_\odot$ central object at a 3.5×10^{-5} M$_\odot$ yr^{-1} rate. A region within 3000 AU is involved in the collapse.

Furthermore, we were able to reconstruct the thermal structure of the envelope between 30 and 5000 AU. The gas temperature tracks the dust temperature very closely in this region. The water is a major coolant through the entire envelope, whereas

CO and OI have relevance only in the outer part of the envelope ($r \geq 300$ AU).

When the dust temperature exceeds 100 K, icy mantles are evaporated injecting in the gas phase more water and ~ 4000 more times of SiO, with respect to the values in the cold part of the envelope. We suggest that molecules like SiO, which are abundant in ices, could be used to trace efficiently the collapse and therefore to identify collapsing protostar candidates.

Acknowledgements. We are grateful to E.van Dishoeck for her comments and helpful discussions on the SiO observations. We acknowledge the dedication of the LWS team which made these observations possible. We thank our referee, F. Shu, for careful reading the manuscript.

References

Adelson L.M., Leung C.M., 1988, MNRAS 235, 349
Bachiller R., 1996, ARA&A 34, 111
Baluteau J.P., Cox P., Cernicharo J., et al., 1997, A&A 322, L33
Blake G.A., van Dishoeck E.F., Jansen D.J., et al., 1994, ApJ 428, 680
Caux E., Ceccarelli C., Castets A., et al., 1999, A&A 347, L1
Ceccarelli C., Hollenbach D.J., Tielens A.G.G.M., 1996, ApJ 471, 400 (CHT96)
Ceccarelli C., Caux E., White G.J., et al., 1998a, A&A 331, 372
Ceccarelli C., Castets A., Loinard L., Caux E., Tielens A.G.G.M., 1998b, A&A 338, L43
Ceccarelli C., Caux E., Loinard L., et al., 1999, A&A 342, L21
Chiar J.E., Adamson A.J., Kerr T.H., Whittet D.C.B., 1995, ApJ 455, 234
Chiar J.E., Gerakines P.A., Whittet D.C.B., et al., 1998, ApJ 498, 716
Clegg P.E.C., Ade P.A.R., Armand C., et al., 1996, A&A 315, L38
Choi M., Evans N.J., Gregersen E.M., Wang Y., 1995, ApJ 448, 742
Doty S.D., Neufeld D.A., 1997, ApJ 489, 122
de Graauw T., Haser L.N., Beintema D.A., et al., 1996, A&A 315, L49
Gerakines P.A., Whittet D.C.B., Ehrenfreund P., et al., 1999, ApJ 522, 357
Gregersen E.M., Evans II N.J., Zhou S., Choi M., 1997, ApJ 484, 256
Kessler M.F., Steinz J.A., Anderegg M.E., et al., 1996, A&A 315, L27
Kraemer K.E., Jackson J.M., Lane A.P., 1998, ApJ 503, 785
Kramer C., Alves J., Lada C.J., et al., 1999, A&A 342, 257
Lee H.-H., Bettens R.P.A., Herbst E., 1996, A&AS 119, 111
Lefloch B., Castets A., Cernicharo J., Langer W.D., Zylka R., 1998, A&A 334, 269
Lefloch B., Castets A., Cernicharo J., Loinard L., 1998, ApJ 504, L109
Leung C.M., Brown R.L. 1977, ApJ 214, L73
Mardones D., Myers P.C., Tafalla M., et al., 1997, ApJ 489, 719
Maréchal P., Pagani L., Langer W.D., Castets A., 1997, A&A 318, 252
Narayanan G., Walker C.K., 1998, ApJ 508, 780
Narayanan G., Walker C.K., Buckley H.D., 1998, ApJ 496, 292
Olofsson G., Pagani L., Tauber J., et al., 1998, A&A 339, L81
Pagani L., Langer W.D., Castets A., 1993, A&A 274, L13
Poglitsch A., Herrmann F., Genzel R., et al., 1996, ApJ 462, L43
Shu F.H., 1977, ApJ 214, 488
Tafalla M., Mardones D., Myers P.C., et al., 1998, ApJ 504, 900
Terebey S., Shu F.H., Cassen P., 1984, ApJ 286, 529
van Dishoeck E.F., Blake G.A., Jansen D.J., Groesbeck T.D., 1995, ApJ 447, 760
van Dishoeck E.F., Blake G.A.. 1998, ARA&A 36, 317
Walker C.K., Lada C.J., Young E.T., Maloney P.R., Wilking B.A., 1986, ApJ 309, L47
Walker C.K., Narayanan G., Boss A.P. 1994, ApJ 431, 767
Williams J.P., Myers P.C., 1999, ApJ 511, 208
Williams J.P., Myers P.C., Wilner D.J., DiFrancesco J., 1999, ApJ 513, L61
Zhou S., 1992, ApJ 394, 204
Zhou S., 1995, ApJ 442, 685